mater.scichina.com link.springer.com

Published online 23 February 2022 | https://doi.org/10.1007/s40843-021-1966-6
Sci China Mater 2022, 65(6): 1679–1686

An ultrahigh fatigue resistant liquid crystal elastomer-based material enabled by liquid metal

Hai-Feng Lu[1,2], Zhen-Zhou Nie[1], Hari Krishna Bisoyi[3], Meng Wang[1], Shuai Huang[1], Xu-Man Chen[1], Zhi-Yang Liu[1] and Hong Yang[1*]

ABSTRACT The low crosslink density characteristic of liquid crystal elastomer (LCE) materials causes poor fatigue resistance performance, which has seriously plagued their prospects in industrial applications. Here we report that the introduction of 5 wt% liquid metal nanodroplets (average diameter: ca. 195 nm) into the LCE network can dramatically reinforce the corresponding composite's mechanical properties, in particular ultrahigh fatigue resistance, capable of bearing unprecedented 10,000 tensile cycles within a large range of strain amplitude up to 70% and 2000 times of continuous actuating deformations. Furthermore, this liquid metal-incorporated LCE composite material exhibits large actuation stroke (maximum actuation strain: 55%), high actuation stress (blocking stress: 1.13 MPa), fully reversible thermal/photo-actuation functions, and self-healing ability at moderate temperatures, which qualifies the composite material for high-load actuators.

Keywords: liquid crystal elastomer, liquid metal, fatigue resistance, actuation

INTRODUCTION

Liquid crystal elastomer (LCE) [1–14], as an extraordinary type of polymeric material combining the anisotropic order of mesogen and the entropy elasticity of elastomer, can exhibit large and reversible shape morphing in response to external stimuli such as heat, light, humidity, electricity, and magnetic field. This remarkable two-way shape memory function endows LCE materials with potential applications in actuators, sensors, micromechanical systems, soft robotic technology, etc. However, conventional LCE materials show unsatisfactory mechanical performances, in particular modest actuation stress and poor fatigue resistance [15–17], which has become the fundamental obstacle impeding the real industrial application of LCE materials. Development of novel LCE materials simultaneously exhibiting large actuation stroke, high actuation stress, and excellent fatigue resistance is highly sought after but remains a formidable challenge.

To improve the mechanical properties of LCE materials, most of the previous studies have focused on enhancing the actuating stress, elastic modulus, and work capacity by introducing new molecular structures, crystallization treatment, interpenetrating network, and the addition of nanofillers [18–23]; however, the fatigue resistance and the long-term durability of LCE materials, a crucial factor for their industrial applications, was barely investigated in the past four decades. This drawback actually derives from the inherent deficiency of LCE structure networks. In order to achieve high actuation strain, LCE materials are always lightly crosslinked. The low crosslink density means that some polymer chains might have no chemical cross-linking, so that during the actuation process the uncrosslinked polymer chains would suffer irreversible slippage, the physical associations of the related polymer chains would be compromised, and parts of molecular network would be permanently damaged [24], resulting in poor fatigue resistance [25].

In order to improve the fatigue resistance of LCE materials, we have tried to incorporate many reinforcing materials such as gold nanoparticles, carbon nanotubes, and carbon fibers into LCE matrices for introducing extra physical associations to strengthen the chain networks of LCEs [21], which however failed in substantially enhancing the fatigue resistance of LCEs. Recently, Ware, Majidi and other scientists described a liquid metal (LM)-doped LCE composite, which could realize electric-driven actuation based on the Joule-heating effect [26–30], and found that the introduction of LM [31–33] fillers into LCE materials could bring many advantages including fluidic nature, negligible toxicity, and flexibility. However, in order to achieve high electrical conductivity for electrothermal conversion, large quantity (~50 vol%) of LM microdroplet (~200 to 500 μm) fillers were incorporated into LCE matrices which did not markedly boost the mechanical performances of the corresponding composites [26]. Decreasing the size of the LM micro-particles to 1–10 μm, although could increase the elastic modulus, sacrificed the most important reversible shape change capability (actuation strain: less than 5%) [27]. Inspired by these pioneering studies, we designed and synthesized a novel LM-incorporated LCE (LM-LCE) material, and astonishingly discovered that a small amount of LM nanodroplets (ca. 5 wt%) could build a strong physical association with LCE networks, affording excellent mechanical performances, in particular ultrahigh fatigue resistance. This LM-LCE material could sustain up to 10,000 tensile

[1] Institute of Advanced Materials, School of Chemistry and Chemical Engineering, State Key Laboratory of Bioelectronics, Southeast University, Nanjing 211189, China
[2] Institute for Science and Applications of Molecular Ferroelectrics, Key Laboratory of the Ministry of Education for Advanced Catalysis Materials, Zhejiang Normal University, Jinhua 321004, China
[3] Advanced Materials and Liquid Crystal Institute and Chemical Physics Interdisciplinary Program, Kent State University, Kent, OH 44242, USA
* Corresponding author (email: yangh@seu.edu.cn)

cycles and achieve more than 2000 times of reversible actuating deformations.

RESULTS AND DISCUSSION

The LM-LCE samples were prepared by using a two-stage *in-situ* thiol-acrylate polymerization/crosslinking method. Most of the previous thiol-acrylate LCEs were fabricated based on RM257 mesogen [17,26–30,34]. White and colleagues [35] recently found that a benzoic acid phenyl ester-based mesogenic core with reduced mesogen-mesogen interaction could enhance and sharpen the thermotropic actuation of the corresponding LCE materials. Here we applied the acrylate-type LC monomer 4-((6-(acryloyloxy)hexyl)oxy)phenyl 4-((6-(acryloyloxy)hexyl)oxy)-benzoate (Y2003). The detailed synthetic protocols are included in the Supplementary information (Figs S1–S5). As schematically illustrated in Fig. 1a, b, the LC monomer Y2003, the chain extender 2,2′-oxybis(ethane-1-thiol), the crosslinker pentaerythritol tetra(3-mercaptopropionate), the catalyst dipropylamine and the LM gallium-indium-tin eutectic alloy (62 wt% Ga, 25 wt% In, and 13 wt% Sn) were mixed in dichloromethane, which gave a transparent solution as shown in Fig. 1c. After ultrasonication for 1 h, the initial transparent solution turned black and achieved a homogeneous mixing of the organic compounds and LMs, which was verified by transmission electron microscopy (TEM) showing that the LM nanodroplets with an average diameter of ca. 195 nm (Fig. 1d) were homogeneously dispersed in the mixture. The above mixture was poured into a polytetrafluoroethylene (PTFE) mold and placed in an oven at 40°C for 1.5 h, the resulting pre-crosslinked LM-LCE sample was uniaxially stretched to ca. 270% of its original length and further kept at 40°C for another 10 h to provide the final LM-LCE material. For comparison purpose, a series of LM-LCE samples with different LM weight percentages (0, 0.5, 1.0, 5.0, 15.0, 25.0 wt%), denoted as LM-LCE-0, LM-LCE-0.5, LM-LCE-1, LM-LCE-5, LM-LCE-15, LM-LCE-25, were also prepared as described in the Supplementary information. Fourier transformed infrared spectroscopy (FT-IR) experiments were carried out to confirm the full conversion of the acrylate and mercapto groups as presented in Fig. S6. The gel fraction experimental results (Fig. S7 and Table S1) also verified the formation of crosslinked polymeric networks. Moreover, we synthesized a micron-sized LM-incorporated LCE composite (denoted as LM-LCE-5-μm) containing 5.0 wt% LM microdroplets with an average diameter of ca. 1.5 μm (Fig. S8), which were prepared by ultrasonication for only 5 min when the initial transparent solution turned gray.

Differential scanning calorimetry (DSC) experiments were carried out to investigate the phase transitions of the LM, pure LCE and LM-LCE samples. As shown in Fig. 2a, the gallium-indium-tin eutectic alloy had only a melting point at ca. 8°C, the LM-LCE-5 composite showed a glass transition (T_g) and an LC-to-isotropic phase transition (T_i) at −24 and 50°C, respectively, on heating, whereas the T_g and T_i of the pure LCE sample were raised to −19 and 55°C, respectively. The melting peak of LM was absent in the composite sample possibly because the solidification and melting temperatures of LM nanodroplets were much lower than those of the bulk LM due to the size effect [36–38]. One-dimensional (1D) and 2D wide-angle X-ray scattering (WAXS) patterns, as presented in Fig. 2b–d, showed that the LM-LCE-5 composite had a nematic liquid crystal phase. The order parameters of the LM-LCE-5 sample at 30°C (nematic phase) and 80°C (isotropic phase) were calculated as ca. 0.72 and 0, respectively, on the basis of the X-ray diffraction (XRD) data (Fig. 2c, d), which indicated a high-quality uniaxial orientation of the mesogens of the LM-LCE-5 sample. The LM-LCE material showed a fully reversible thermally induced deformation as illustrated in Fig. 2e and Supplementary information Movie S1. The actuating stress of LM-LCE-5 material was examined on a

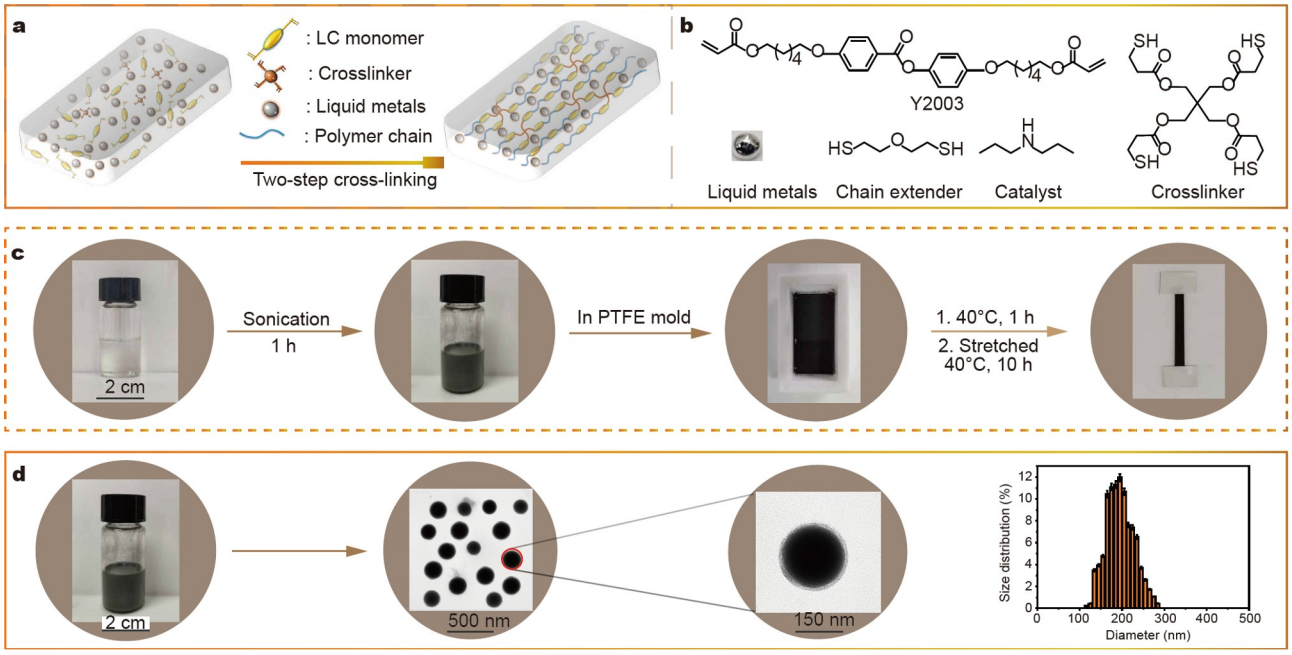

Figure 1 (a) Schematic illustration of the preparation protocol of LM-LCE materials. (b) The molecular structures of LC monomer, LM, chain extender, catalyst and crosslinker. (c) The photo images of the monomeric mixture solution before and after sonication for 1 h, the pre-crosslinking process in a PTFE mold and the final uniaxial-aligned LM-LCE-5 film. (d) TEM images and size distribution of LM nanodroplets in the LM-LCE-5 solution composite.

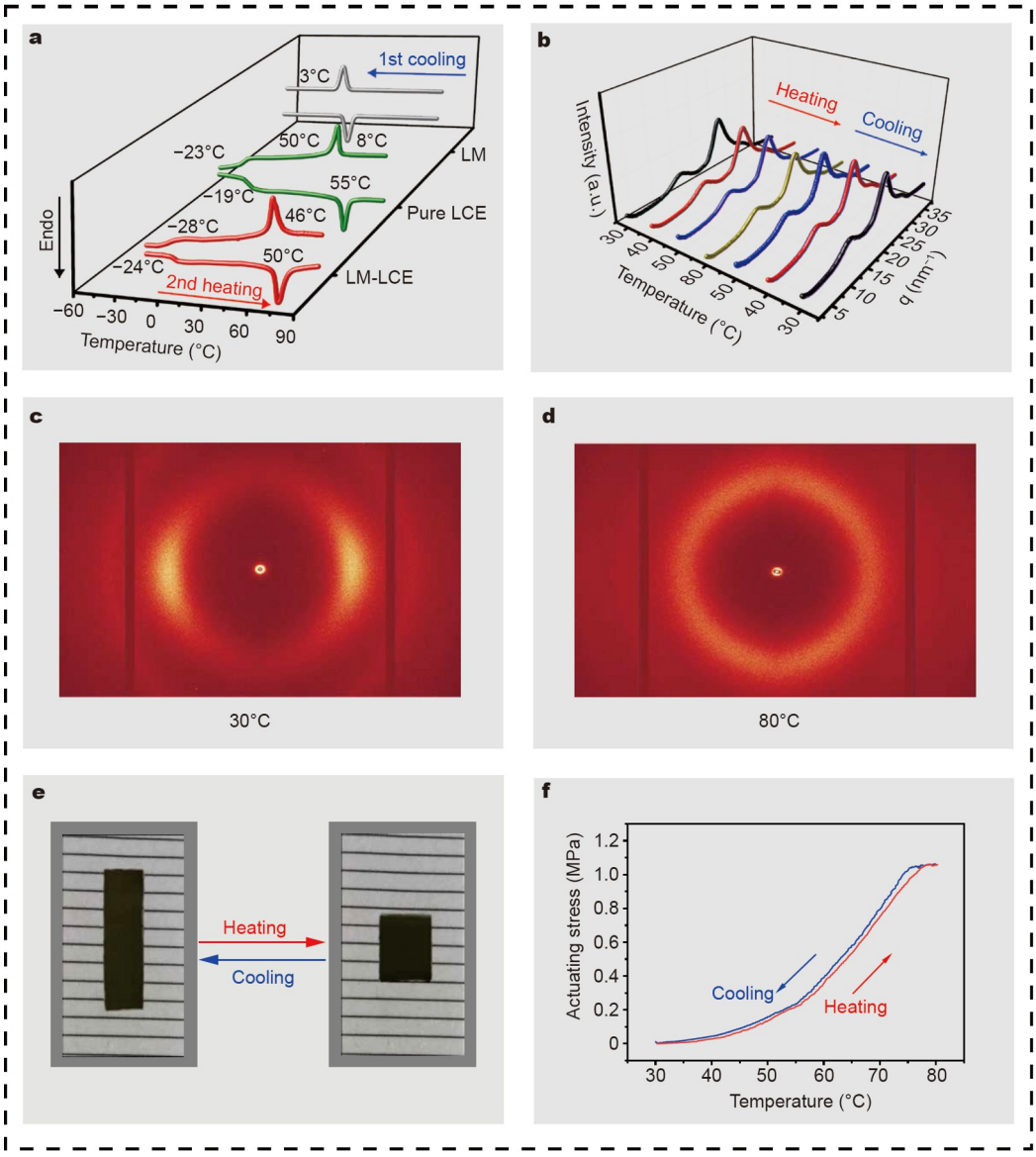

Figure 2 (a) DSC thermograms of LM, LM-LCE-5 and pure LCE samples on heating and cooling processes. (b) 1D-WAXS patterns of the LM-LCE-5 sample measured on heating and cooling processes. 2D-WAXD patterns of the LM-LCE-5 sample measured at (c) 30°C and (d) 80°C. (e) Two-way shape-morphing behavior and (f) representative isostrain (0.01%) measurement of the LM-LCE-5 film.

dynamic mechanical analyzer (DMA Q850, TA Instrument). The generated contractile force of the LM-LCE-5 sample measured under 0.01% isostrain mode was plotted against the temperature variation (Fig. 2f), showing that the blocking (maximum) stress of the composite film reached 1.13 MPa, which was comparable to the values of conventional LCE materials (0.45–1.3 MPa) [18,19].

The linear viscoelastic regimes (elastic strain range, where the storage modulus E' and the loss modulus E'' remain constant) of the pure LCE and LM-LCE composites were first determined by dynamic strain sweep experiments [39]. As shown in Fig. 3a–c, three representative LCE ribbons LM-LCE-0, LM-LCE-5-μm and LM-LCE-5 held between two DMA tension clamps, appeared in three different colors (white, gray and black) due to the size-dependent surface plasmon resonance effect of the included LM micro- and nano-droplets [40]. As illustrated in Fig. 3d–f and Fig. S9, the elastic strain of pure LCE sample was about 3.8%. With the addition of LM nanodroplets, LM-LCE samples showed an enhanced elastic strain; in particular, the LM-LCE-5 sample presented a 72.2% elastic strain, which is much higher than that of pure LCE, whereas the LM-LCE-5-μm sample with micron-sized LM fillers, in a sharp contrast, presented a 13.6% elastic strain. The fatigue resistance properties of these LM-LCE samples were first examined by the dynamic uniaxial cyclic loading experiments within their linear viscoelastic regimes, the loading strain and the strain rate were set as 1% and 10 mm min^{-1}, respectively. The representative uniaxial tensile stress-strain curves with loading-unloading cycles of the pure LCE and LM-LCE composite samples are displayed in Fig. 3g–i and Fig. S10. Compared with the traditional pure LCE sample which lost its mechanical property rapidly since the first loading-unloading cycle and was damaged after only 396 and 1561 cycles, respectively (Fig. 3g, h), the LM-LCE-5 material exhibited extraordinarily superior fatigue resistance. As shown

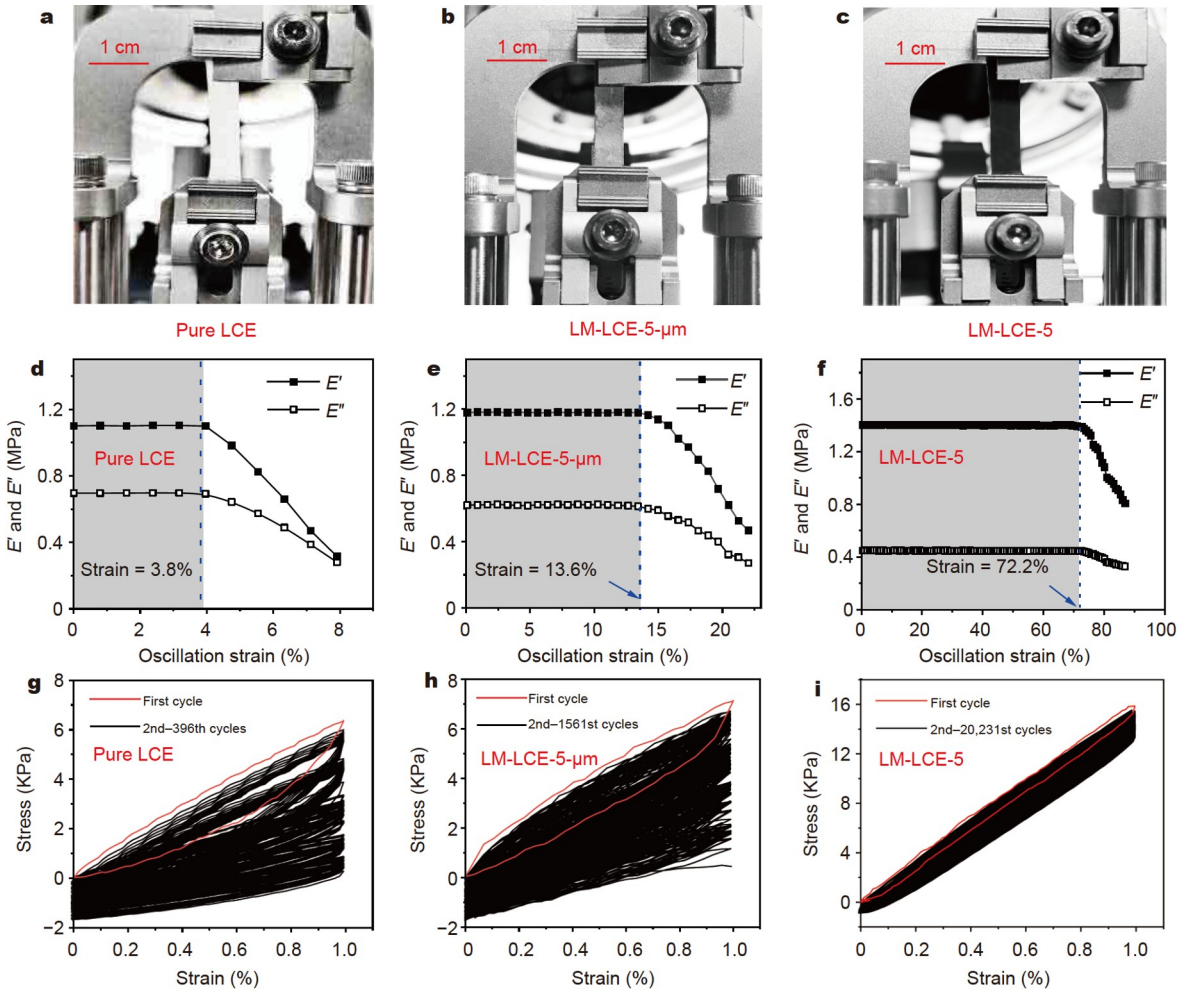

Figure 3 Photo images of (a) pure LCE, (b) LM-LCE-5-μm and (c) LM-LCE-5 samples subjected to dynamic uniaxial tensile testing. Storage modulus (E') and loss modulus (E'') *versus* oscillation strain curves of (d) pure LCE, (e) LM-LCE-5-μm and (f) LM-LCE-5 samples (the frequency was set as 1 Hz). Representative uniaxial tensile stress-strain curves with loading-unloading cycles of (g) pure LCE, (h) LM-LCE-5-μm and (i) LM-LCE-5 samples.

in Fig. 3i, a slight inelastic deformation of the LM-LCE-5 sample was found in the first loading cycle, which was attributed to Mullins effect [41].

For the subsequent loadings, the mechanical performance of LM-LCE-5 sample remained stable even after 20,000 loading-unloading cycles, and exhibited much smaller hysteresis. Since the actual application of LCE material usually requires high strain rate, the fatigue resistance properties of these LM-LCE composites were further examined with a much higher loading strain of 70%, as shown in Fig. 4 and Fig. S11. Meanwhile, the infrared images (Fig. 4a–c) of the examined samples were taken during the dynamic uniaxial tensile testing. As illustrated in Fig. 4d, e, beyond their linear viscoelastic regimes, the pure LCE sample and LM-LCE-5-μm composite would be quickly damaged after 72 and 632 loading-unloading cycles respectively, whereas the LM-LCE-5 material could preserve its mechanical property even after 10,000 loading-unloading cycles (Fig. 4f). The dissipation energy and the dissipation coefficients of pure LCE, LM-LCE-5-μm and LM-LCE-5 samples in the uniaxial cyclic loading process were also analyzed. As shown in Fig. 4g–i, the dissipation energy and coefficient of LM-LCE-5 maintained stable values of ca. 20 kJ m^{-3} and 10%, respectively, after 10,000 loading-unloading cycles, whereas those two values of pure LCE and LM-LCE-5-μm samples dropped dramatically from 60 kJ m^{-3} and 40%, 51.2 kJ m^{-3} and 38.6%, to 20 kJ m^{-3} and 28%, 20.2 kJ m^{-3} and 22.9% after 72 and 632 loading cycles, respectively.

Furthermore, the mechanical properties of other LM-LCE samples with different LM weight percentages were also investigated. As shown in Table 1 and Fig. S12, although the mechanical performances of all the LM-incorporated LCE composites outweighed those of pure LCE material, the optimal values of LM-LCE material appeared when the weight percentage of nanometer-sized LM reached 5 wt%, and the toughness (determined by the integral area under the stress-strain curve measured in quasi-static tensile experiments [42,43]), elastic modulus, failure strain and ultimate strength were recorded as 18.31 MJ m^{-3}, 2.01 MPa, 1010.9% and 3.67 MPa respectively.

The superior fatigue resistance of LM-LCE material might derive from two aspects: (1) the fluidic and soft LM nanodroplets could serve as stress concentration points and effectively help the dissipation of the generated deformation energy which was transformed into heat [44]. This hypothesis could be partially confirmed by the infrared images of LM-LCE sample which had a much lower surface temperature than the pure LCE sample even after thousand times of uniaxial tensile stress, as

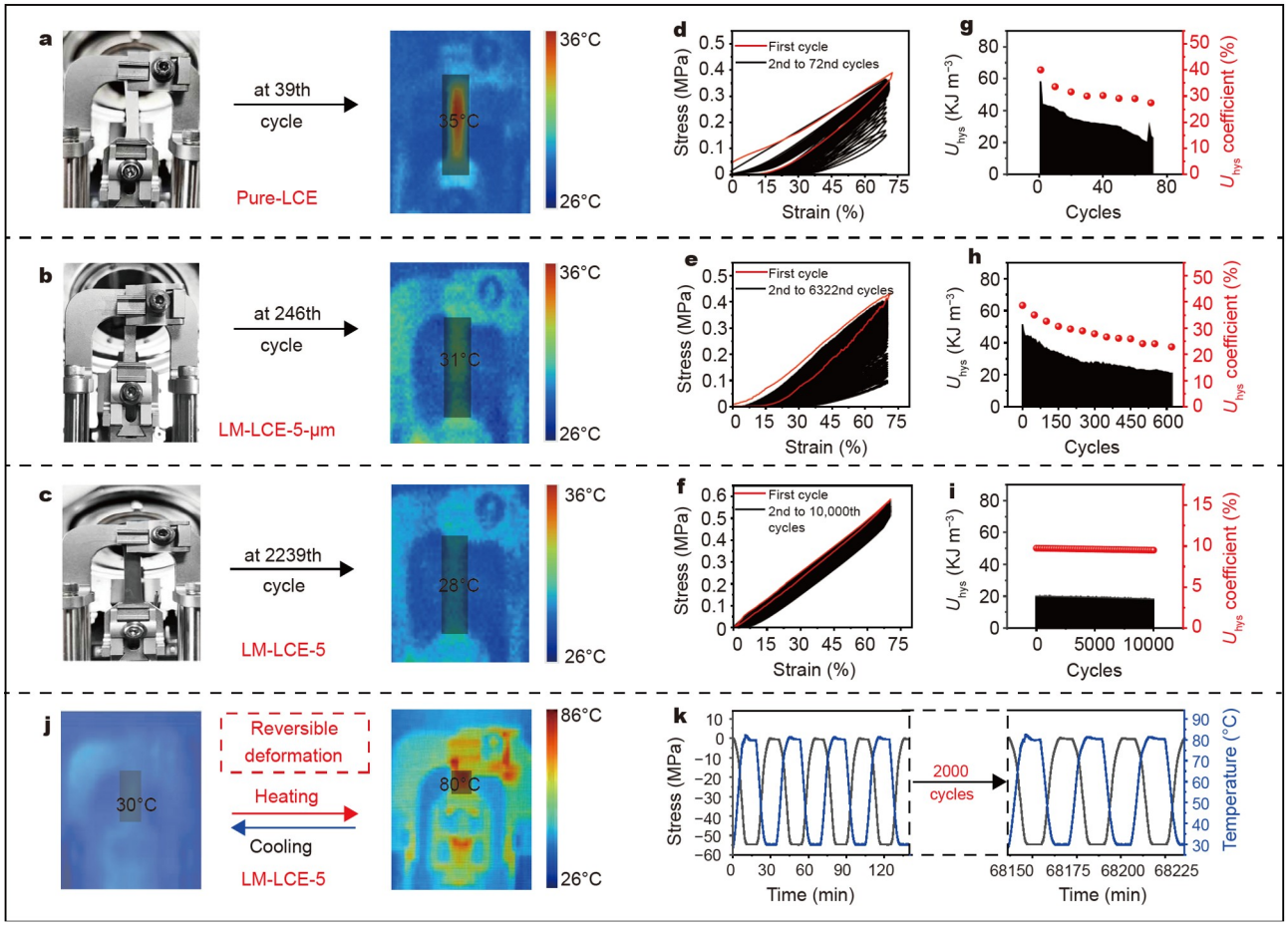

Figure 4 Photos and thermal infrared images of (a) pure LCE, (b) LM-LCE-5-μm and (c) LM-LCE-5 samples subjected to dynamic uniaxial tensile testing. Representative uniaxial tensile stress-strain curves with loading-unloading cycles (within 70% strain) of (d) pure LCE, (e) LM-LCE-5-μm and (f) LM-LCE-5 samples. The dissipation energy and the dissipation coefficients of representative uniaxial tensile stress-strain curves with loading-unloading cycles (within 70% strain) of (g) pure LCE, (h) LM-LCE-5-μm and (i) LM-LCE-5 samples. (j) Infrared images of LM-LCE-5 in the reversible deformation process examined using the isoforce mode. (k) The strain (in isoforce mode) and temperature diagram of LM-LCE-5 film recorded in 2000 continuous actuation cycles.

Table 1 Mechanical properties of LM-LCE and pure LCE samples

LCE sample	Uniaxial cyclic loading (cycles)[a]	Uniaxial cyclic loading (cycles)[b]	Toughness (MJ m^{-3})[c]	Elastic modulus (MPa)[c]	Failure strain (%)[c]	Ultimate strength (MPa)[c]
LM-LCE-0	396	72	0.30	0.89	95.0	1.01
LM-LCE-0.5	672	296	0.79	1.01	134.1	1.25
LM-LCE-1	3571	1632	1.75	1.27	213.2	1.77
LM-LCE-5	20,231	10,000	18.31	2.01	1010.9	3.67
LM-LCE-5-μm	1561	632	2.04	1.03	239.5	1.89
LM-LCE-15	1942	1532	5.45	0.78	463.4	2.38
LM-LCE-25	979	481	1.28	0.36	238.2	1.35

a) Uniaxial stretching to 1% strain and releasing, measured in dynamic tensile experiments. b) Uniaxial stretching to 70% strain and releasing, measured in dynamic tensile experiments. c) Measured in quasi-static tensile experiments.

shown in Fig. 4a–c and Fig. S13. (2) The polymer chains could be anchored onto the LM surfaces through metal-sulfur interaction [45], which might further afford extra physical associations to reinforce the LCE network and improve the shape deformation recovery capacity to some extent. Owing to the affinity between metal and sulfur, the LM nanodroplets were uniformly dispersed in the LM-LCE-5 sample as shown in the scanning electron microscopy (SEM) images (Figs S14 and S15). The energy-dispersive X-ray spectroscopy (EDS) image (Fig. S16) further indicated the uniform dispersions of gallium and sulfur elements in the LM-LCE composite. However, if more LM nanodroplets or micron-sized LM droplets were added into the composites, LM particles would gradually aggregate in the LCE matrix, as illustrated in Fig. S17.

In addition to its excellent fatigue resistance, the LM-LCE-5 material also exhibited prominent reversible thermal-actuation

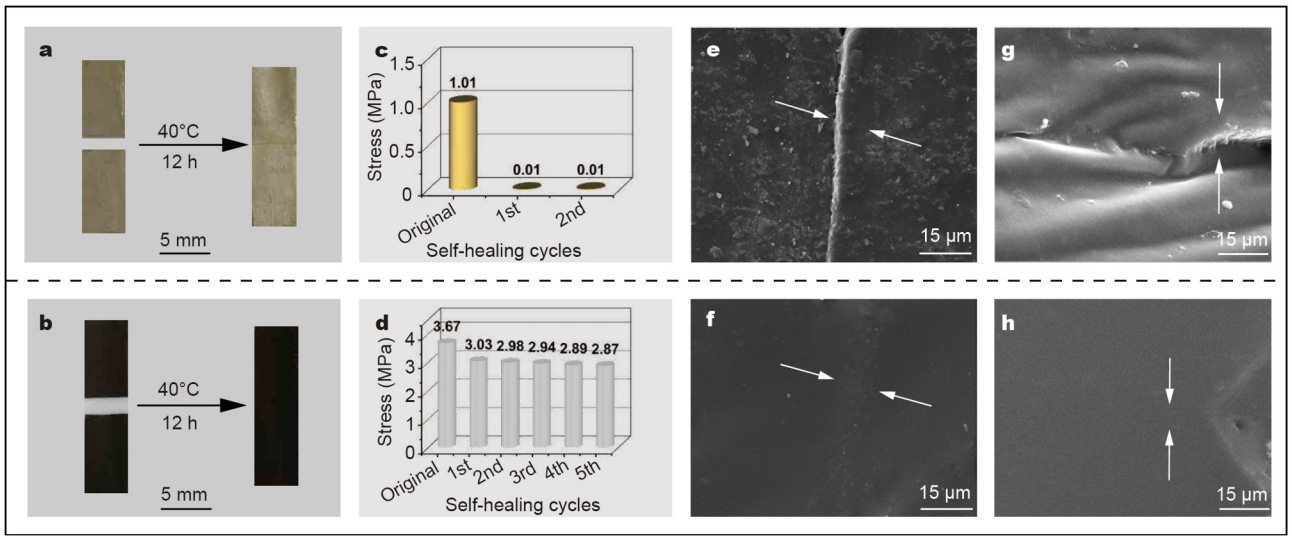

Figure 5 The photographs of (a) LM-LCE-0 and (b) LM-LCE-5 ribbons for self-healing examinations. Tensile stress experiments of (c) LM-LCE-0 and (d) LM-LCE-5 ribbons in repeated cut/heal cycles (40°C, 12 h). The surface SEM images of the reattached (e) LM-LCE-0 and (f) LM-LCE-5 ribbons after the self-healing treatment (40°C, 12 h). The cross-section SEM images of (g) LM-LCE-0 and (h) LM-LCE-5 ribbons after the self-healing treatment (40°C, 12 h).

capacity. As shown in Movie S1, directly heating an LM-LCE-5 ribbon on a temperature-controlled hot stage caused a maximum shrinking strain of ca. 55% in the nematic-to-isotropic phase transition. The continuous reversible shape morphing capacity of the LM-LCE-5 material was further investigated by DMA testing under the isoforce mode using a 0.005 N preload static force, as demonstrated in Fig. 4j. The strain diagram of the LM-LCE-5 ribbon was recorded for 2000 continuous heating-cooling cycles, which showed an incredibly steady actuation performance. Moreover, thanks to the ultraviolet (UV)-excitation photothermal effect of LM nanodroplets (see Figs S18 and S19), the corresponding LM-LCE material could also be photo-actuated by UV light as shown in Fig. S20 and Movie S2.

Besides the above thermal/photo-actuation functionalities [46,47], the LM-LCE material exhibited good self-healing capability under mild conditions. For the traditional LCE materials based on dynamic chemical bonds, the complete healing usually requires high temperature [48–50], which is apparently not suitable for real industrial applications. In sharp contrast, the LM-LCE composites could effectively self-heal at 40°C. As shown in Fig. 5a, b, two ribbons LM-LCE-0 and LM-LCE-5 (ca. 21.5 mm long × 4.4 mm wide × 410 μm thick) were cut in half and reattached respectively, and further kept at 40°C for 12 h. After being cooled to room temperature, the samples were examined by the quasi-static tensile experiments on an SANS E42.503 tensile tester as illustrated in Fig. S21. The ultimate strengths of the two reattached ribbons as described in Fig. 5c, d revealed that pure LCE material had no self-healing effect at all, whereas the LM-LCE-5 sample exhibited ca. 80% average healing efficiency (defined as the tensile strength ratio of the self-healed sample to the original sample) in 5 repeated cut/heal cycles.

The SEM images of the self-healed LM-LCE-5 sample also proved the superior self-healing property. Compared with the distinct cracks which were observed in the surface (Fig. 5e) and cross-section (Fig. 5g) of the reattached LM-LCE-0 sample, almost no obvious damage could be visualized in the surface (Fig. 5f) and cross-section (Fig. 5h) of the self-healed LM-LCE-5 material. These results are consistent with the observation in optical microscope as shown in Fig. S22. The self-healing property of LM-LCE-5 sample might be attributed to the dynamic reassociation of metal and sulfur [51], which could be verified by the tensile relaxation experiments [50,52] as shown in Fig. S23.

CONCLUSIONS

In summary, we found that the introduction of a small amount of LM nanodroplets into LCE network could dramatically reinforce the corresponding composite's mechanical property, in particular ultrahigh fatigue resistance, capable of bearing 10,000 tensile cycles with a loading strain of 70% and 2000 times of continuous actuating deformations. Moreover, this novel LM-LCE composite material exhibited large actuation stroke (maximum actuation strain: ~55%), high actuation stress (blocking stress: ~1.13 MPa), fully reversible thermal/photo-actuation functions, and good self-healing ability at moderate temperatures, which would make it an ideal candidate for high-load actuators. The responsive material system developed and disclosed here could find applications in actuators, microfluidics, soft robotics, and beyond. Furthermore, we hope that this discovery could provide a new impetus for the community to inch toward the long-term desired industrial utilizations of LCE materials.

Received 18 November 2021; accepted 10 January 2022; published online 23 February 2022

1 Finkelmann H, Kock HJ, Rehage G. Investigations on liquid crystalline polysiloxanes 3. Liquid crystalline elastomers—A new type of liquid crystalline material. Makromol Chem Rapid Commun, 1981, 2: 317–322
2 Ohm C, Brehmer M, Zentel R. Liquid crystalline elastomers as actuators and sensors. Adv Mater, 2010, 22: 3366–3387
3 Ube T, Ikeda T. Photomobile polymer materials with crosslinked liquid-crystalline structures: Molecular design, fabrication, and functions. Angew Chem Int Ed, 2014, 53: 10290–10299
4 White TJ, Broer DJ. Programmable and adaptive mechanics with liquid crystal polymer networks and elastomers. Nat Mater, 2015, 14: 1087–

1098
5 Bisoyi HK, Li Q. Light-driven liquid crystalline materials: From photo-induced phase transitions and property modulations to applications. Chem Rev, 2016, 116: 15089–15166
6 Kularatne RS, Kim H, Boothby JM, *et al.* Liquid crystal elastomer actuators: Synthesis, alignment, and applications. J Polym Sci Part B-Polym Phys, 2017, 55: 395–411
7 Li Q, Schenning APHJ, Bunning TJ. Light-responsive smart soft matter technologies. Adv Opt Mater, 2019, 7: 1901160
8 Dong L, Zhao Y. Photothermally driven liquid crystal polymer actuators. Mater Chem Front, 2018, 2: 1932–1943
9 Hu J, Wang W, Yu H. Endowing soft photo-actuators with intelligence. Adv Intelligent Syst, 2019, 1: 1900050
10 Yang M, Yuan Z, Liu J, *et al.* Photoresponsive actuators built from carbon-based soft materials. Adv Opt Mater, 2019, 7: 1900069
11 Jiang ZC, Xiao YY, Zhao Y. Shining light on liquid crystal polymer networks: Preparing, reconfiguring, and driving soft actuators. Adv Opt Mater, 2019, 7: 1900262
12 Ube T, Ikeda T. Photomobile polymer materials with complex 3D deformation, continuous motions, self-regulation, and enhanced processability. Adv Opt Mater, 2019, 7: 1900380
13 Mehta K, Peeketi AR, Liu L, *et al.* Design and applications of light responsive liquid crystal polymer thin films. Appl Phys Rev, 2020, 7: 041306
14 Ge F, Zhao Y. Microstructured actuation of liquid crystal polymer networks. Adv Funct Mater, 2020, 30: 1901890
15 Thomsen DL, Keller P, Naciri J, *et al.* Liquid crystal elastomers with mechanical properties of a muscle. Macromolecules, 2001, 34: 5868–5875
16 Beyer P, Terentjev EM, Zentel R. Monodomain liquid crystal main chain elastomers by photocrosslinking. Macromol Rapid Commun, 2007, 28: 1485–1490
17 Wang Z, Li K, He Q, *et al.* A light-powered ultralight tensegrity robot with high deformability and load capacity. Adv Mater, 2019, 31: 1806849
18 Yang R, Zhao Y. Multitemperature memory actuation of a liquid crystal polymer network over a broad nematic-isotropic phase transition induced by large strain. ACS Macro Lett, 2018, 7: 353–357
19 Kim H, Boothby JM, Ramachandran S, *et al.* Tough, shape-changing materials: Crystallized liquid crystal elastomers. Macromolecules, 2017, 50: 4267–4275
20 Lu HF, Wang M, Chen XM, *et al.* Interpenetrating liquid-crystal polyurethane/polyacrylate elastomer with ultrastrong mechanical property. J Am Chem Soc, 2019, 141: 14364–14369
21 Liu J, Gao Y, Wang H, *et al.* Shaping and locomotion of soft robots using filament actuators made from liquid crystal elastomer-carbon nanotube composites. Adv Intelligent Syst, 2020, 2: 1900163
22 Song T, Lei H, Clancy AJ, *et al.* Supramolecular hydrogen bond enables Kapton nanofibers to reinforce liquid-crystalline polymers for light-fueled flight. Nano Energy, 2021, 87: 106207
23 Wang J, Huang S, Zhang Y, *et al.* Hydrogen bond enhances photo-mechanical swing of liquid-crystalline polymer bilayer films. ACS Appl Mater Interfaces, 2021, 13: 6585–6596
24 Haque MA, Kurokawa T, Kamita G, *et al.* Lamellar bilayers as reversible sacrificial bonds to toughen hydrogel: Hysteresis, self-recovery, fatigue resistance, and crack blunting. Macromolecules, 2011, 44: 8916–8924
25 Lee KY, Rowley JA, Eiselt P, *et al.* Controlling mechanical and swelling properties of alginate hydrogels independently by cross-linker type and cross-linking density. Macromolecules, 2000, 33: 4291–4294
26 Ford MJ, Ambulo CP, Kent TA, *et al.* A multifunctional shape-morphing elastomer with liquid metal inclusions. Proc Natl Acad Sci USA, 2019, 116: 21438–21444
27 Ford MJ, Palaniswamy M, Ambulo CP, *et al.* Size of liquid metal particles influences actuation properties of a liquid crystal elastomer composite. Soft Matter, 2020, 16: 5878–5885
28 Style RW, Wettlaufer JS, Dufresne ER. Surface tension and the mechanics of liquid inclusions in compliant solids. Soft Matter, 2015, 11: 672–679
29 Kazem N, Hellebrekers T, Majidi C. Soft multifunctional composites and emulsions with liquid metals. Adv Mater, 2017, 29: 1605985
30 Style RW, Boltyanskiy R, Allen B, *et al.* Stiffening solids with liquid inclusions. Nat Phys, 2015, 11: 82–87
31 Yu Q, Zhang Q, Zong J, *et al.* Identifying surface structural changes in a newly-developed Ga-based alloy with melting temperature below 10 °C. Appl Surf Sci, 2019, 492: 143–149
32 Koh A, Hwang W, Y. Zavalij P, *et al.* Solidification and melting phase change behavior of eutectic gallium-indium-tin. Materialia, 2019, 8: 100512
33 Handschuh-Wang S, Stadler FJ, Zhou X. Critical review on the physical properties of gallium-based liquid metals and selected pathways for their alteration. J Phys Chem C, 2021, 125: 20113–20142
34 Yakacki CM, Saed M, Nair DP, *et al.* Tailorable and programmable liquid-crystalline elastomers using a two-stage thiol-acrylate reaction. RSC Adv, 2015, 5: 18997–19001
35 McCracken JM, Donovan BR, Lynch KM, *et al.* Molecular engineering of mesogenic constituents within liquid crystalline elastomers to sharpen thermotropic actuation. Adv Funct Mater, 2021, 31: 2100564
36 Avsar A, Ciarrocchi A, Pizzochero M, *et al.* Defect induced, layer-modulated magnetism in ultrathin metallic $PtSe_2$. Nat Nanotechnol, 2019, 14: 674–678
37 Yamaguchi A, Mashima Y, Iyoda T. Reversible size control of liquid-metal nanoparticles under ultrasonication. Angew Chem Int Ed, 2015, 54: 12809–12813
38 Yarema M, Wörle M, Rossell MD, *et al.* Monodisperse colloidal gallium nanoparticles: Synthesis, low temperature crystallization, surface plasmon resonance and Li-ion storage. J Am Chem Soc, 2014, 136: 12422–12430
39 Frohm B, DeNizio JE, Lee DSM, *et al.* A peptide from human semenogelin I self-assembles into a pH-responsive hydrogel. Soft Matter, 2015, 11: 414–421
40 Juvé V, Cardinal MF, Lombardi A, *et al.* Size-dependent surface plasmon resonance broadening in nonspherical nanoparticles: Single gold nanorods. Nano Lett, 2013, 13: 2234–2240
41 Bartlett MD, Kazem N, Powell-Palm MJ, *et al.* High thermal conductivity in soft elastomers with elongated liquid metal inclusions. Proc Natl Acad Sci USA, 2017, 114: 2143–2148
42 Kazem N, Bartlett MD, Majidi C. Extreme toughening of soft materials with liquid metal. Adv Mater, 2018, 30: 1706594
43 Zhang J, Liu M, Pearce G, *et al.* Strain stiffening and positive piezoconductive effect of liquid metal/elastomer soft composites. Compos Sci Tech, 2021, 201: 108497
44 Peng H, Xin Y, Xu J, *et al.* Ultra-stretchable hydrogels with reactive liquid metals as asymmetric force-sensors. Mater Horiz, 2019, 6: 618–625
45 Griebel JJ, Glass RS, Char K, *et al.* Polymerizations with elemental sulfur: A novel route to high sulfur content polymers for sustainability, energy and defense. Prog Polym Sci, 2016, 58: 90–125
46 Ambulo CP, Ford MJ, Searles K, *et al.* 4D-printable liquid metal-liquid crystal elastomer composites. ACS Appl Mater Interfaces, 2021, 13: 12805–12813
47 Lv P, Yang X, Bisoyi HK, *et al.* Stimulus-driven liquid metal and liquid crystal network actuators for programmable soft robotics. Mater Horiz, 2021, 8: 2475–2484
48 Pei Z, Yang Y, Chen Q, *et al.* Mouldable liquid-crystalline elastomer actuators with exchangeable covalent bonds. Nat Mater, 2014, 13: 36–41
49 Li Y, Zhang Y, Rios O, *et al.* Liquid crystalline epoxy networks with exchangeable disulfide bonds. Soft Matter, 2017, 13: 5021–5027
50 Wang Z, Tian H, He Q, *et al.* Reprogrammable, reprocessible, and self-healable liquid crystal elastomer with exchangeable disulfide bonds. ACS Appl Mater Interfaces, 2017, 9: 33119–33128
51 Xin Y, Peng H, Xu J, *et al.* Ultrauniform embedded liquid metal in sulfur polymers for recyclable, conductive, and self-healable materials. Adv Funct Mater, 2019, 29: 1808989
52 Niu W, Cao X, Wang Y, *et al.* Photonic vitrimer elastomer with self-healing, high toughness, mechanochromism, and excellent durability based on dynamic covalent bond. Adv Funct Mater, 2021, 31: 2009017

Acknowledgements This work was supported by the National Natural Science Foundation of China (21971037).

Author contributions Yang H designed this project; Lu HF performed all the experiments; Lu HF, Nie ZZ, Bisoyi HK, Wang M, Huang S, Chen XM, Liu ZY and Yang H analyzed the data and wrote the manuscript. All authors contributed to the general discussion.

Conflict of interest The authors declare that they have no conflict of interest.

Supplementary information Experimental details and supporting data are available in the online version of the paper.

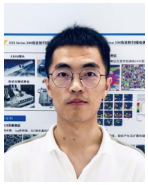

Hai-Feng Lu completed his PhD degree under the supervision of Prof. Hong Yang in 2021. After that, he joined Zhejiang Normal University as a lecturer. His research interest includes functional polymeric materials.

Hong Yang is professor of chemistry and chemical engineering at Southeast University. He earned his BS degree in chemistry from Peking University in 2002, and his PhD degree in chemistry from the University of Colorado at Boulder in 2007 with Prof. David M Walba. After one year industry work as a research scientist of medicinal chemistry in a Chicago pharmaceutical company, he went back to academia and joined Dr. Patrick Keller's group at Institut Curie in 2008. Since completing his postdoctoral research in the spring of 2010, he has been a faculty at Southeast University. Currently, his research interests are liquid crystal materials and functional polymeric materials.

具有超高抗疲劳性能的液态金属增强型液晶弹性体材料

陆海峰[1,2], 聂振洲[1], Hari Krishna Bisoyi[3], 王猛[1], 黄帅[1], 陈旭浸[1], 刘志洋[1], 杨洪[1*]

摘要 液晶弹性体材料内在的低交联密度特性导致其抗疲劳性能差, 严重影响了此类材料在工业上的应用前景. 本文报道了一种液态金属增强型液晶弹性体材料, 通过将5 wt%液态金属纳米微粒(平均直径: 约195 nm)引入液晶弹性体网络, 可以显著增强液晶弹性体复合材料的力学性能, 特别是超高的抗疲劳性能. 该复合材料能够在大应变范围(应变幅度范围高达70%)内承受10,000次拉伸循环和2000次连续可逆致动形变, 同时展现出大致动应变(最大致动应变: 55%)、大致动应力(1.13 MPa)、完全可逆的热/光驱动性和常温下的自修复功能. 该液态金属增强型液晶弹性体材料有望在高载荷致动器领域实现工业化应用.

